RESEARCH ARTICLE | DECEMBER 30 2024

Analysis of the effect of the Fermi surface matching at Co–Fe and Cu interface on giant magnetoresistance effect using a combinatorial technique

Varun Kumar Kushwaha ; Ryo Toyama ; Yoshio Miura ; Yuma Iwasaki ; Yuya Sakuraba

AIP Advances 14, 125329 (2024)
https://doi.org/10.1063/5.0216909
CHORUS

Analysis of the effect of the Fermi surface matching at Co–Fe and Cu interface on giant magnetoresistance effect using a combinatorial technique

Cite as: AIP Advances 14, 125329 (2024); doi: 10.1063/5.0216909
Submitted: 24 June 2024 • Accepted: 27 November 2024 •
Published Online: 30 December 2024

Varun Kumar Kushwaha,[1,a),b)] Ryo Toyama,[1] Yoshio Miura,[1] Yuma Iwasaki,[2] and Yuya Sakuraba[1,a)]

AFFILIATIONS

[1] Research Center for Magnetic and Spintronic Materials, National Institute for Materials Science, 1-2-1 Sengen, Tsukuba 305-0047, Japan
[2] Center for Basic Research on Materials, National Institute for Materials Science, 1-1 Namiki, Tsukuba 305-0044, Japan

[a)] **Authors to whom correspondence should be addressed:** KUSHWAHA.Varun.Kumar.d8@tohoku.ac.jp, and SAKURABA.Yuya@nims.go.jp
[b)] **Current address:** Institute for Materials Research, Tohoku University, Aoba, Sendai 980-8577, Japan.

ABSTRACT

Interfacial electronic band-matching (EBM) plays a crucial role in determining the spin-dependent transport properties and performance of spintronic devices. The final goal of this study is to establish a method to search for new material combinations that exhibit favorable EBM at the interfaces to achieve a superior performance in various spintronic devices using the machine learning technique combined with the first-principles calculations. As a first step, we investigate the effect of interfacial EBM on magnetoresistance (MR) by fabricating the current-in-plane giant magnetoresistive devices with compositionally graded $Co_{1-\beta}Fe_{\beta}$ layers and Cu spacer. The MR ratio varies significantly across β = 0.11–1.0, with the highest MR of 17.5% observed at $\beta \approx 0.46$, followed by a sharp decrease beyond β = 0.6. To analyze the β dependence of MR in terms of EBM with low computational cost, we calculate the simple Fermi surfaces of bcc $Co_{1-\beta}Fe_{\beta}$ and Cu and evaluate the wave number (k) distance between their Fermi surfaces. The closest (furthest) Fermi surface match occurs at $\beta \approx 0.4$ (1.0), which tends to be in good agreement with the observed MR trend. This suggests that a simple Fermi surface similarity analysis, when integrated with a machine learning technique, can be an effective method for efficiently identifying new material combinations with high EBM.

I. INTRODUCTION

In recent years, the combination of first-principles calculations and machine-learning techniques has emerged as a powerful high-throughput approach for discovering novel materials and composite structures with desirable properties from vast exploration spaces.[1–10] This approach has been successfully applied in the field of magnetism and spintronics research to predict unknown materials with significant magnetization and spin polarization, of which some have been experimentally demonstrated.[1,2,11] However, for spin-dependent transport phenomena in the heterojunction with a magnetic material, such as giant-magnetoresistance (GMR), tunnel-magnetoresistance, spin-pumping, and spin–orbit torque, the transport characteristics depend not only on the bulk properties of the materials but also on the properties of the interfaces between magnetic and non-magnetic materials, specifically the interface electronic band-matching (EBM).[12–21] For example, in current-perpendicular-to-plane (CPP) GMR devices composed of stacked multilayer structures of magnetic and non-magnetic layers, it is well understood that the magnetoresistance (MR) ratio is determined not only by the spin-polarization in the bulk region of magnetic layers but also by the interfacial spin polarization.[22] However, performing calculations for the transport properties involving interfaces is computationally expensive[12,16,18–21] and not suitable for rapidly generating sufficient data for machine learning purposes due to the need to perform first-principles electronic and transport calculations for the supercells of ferromagnetic and non-magnetic multilayers.

Therefore, the development of a new theoretical method for the prediction of EBM in heterogeneous materials is crucial for realizing a high-throughput approach using the machine learning technique. In addition, it is desirable to establish an efficient experimental method for fabricating the interfaces of heterogeneous materials of various compositions and structures to verify the predictions made by this new theoretical method.

Recently, Fathoni *et al.* reported that (001)-oriented epitaxial $Co_{50}Fe_{50}$/metastable body-centered cubic (bcc)-Cu/$Co_{50}Fe_{50}$ current-in-plane (CIP)-GMR gives the highest MR ratio ever reported, 40.5% at room temperature (RT) in the trilayer CIP-GMR film, in the history of the study of CIP-GMR.[19] The first-principles calculation of the in-plane momentum ($k_{//}$) dependence of the majority and minority spin electron transmittance has revealed that the high (tiny) transmittance of the majority (minority) spin electron near the edges (whole) of Brillouin zone (BZ) is essential for a high MR ratio.[19,21] Although it had been well known that there must be a similarity in the density of state of one spin-channel between the magnetic material and non-magnetic material for obtaining a high MR ratio in CIP-GMR devices, they have clearly demonstrated for the first time the importance of $k_{//}$ dependence of EBM for CIP-GMR.

As a Co–Fe binary alloy forms the bcc structure with nearly the same lattice constant over a wide composition range, in this study, we selected an epitaxial Co–Fe/Cu/Co–Fe CIP-GMR device as a simple model system to explore a new efficient theoretical approach for investigating the interface $k_{//}$ dependence of EBM. Considering the challenges associated with fine-tuning the composition of Co–Fe layer and the thickness of Cu spacer using conventional deposition methods, we employed the combinatorial sputtering technique using a linear-motion mask.[1,23–31] This allows us to fabricate Co–Fe/Cu/Co–Fe CIP-GMR devices with composition-graded Co–Fe layers and a thickness-graded Cu spacer.

The final goal of this study is to establish a new method for discovering new material combinations that exhibit high interfacial EBM for CIP- and CPP-GMR through the integration of machine-learning techniques and first-principles calculations. In the present study, as a first step toward this goal, we aim to verify the analyzability of experimental results from Co–Fe/Cu/Co–Fe CIP-GMR devices through simple Fermi surface calculations, which are computationally much less expensive compared to conventional calculations of spin-dependent transmission.

II. METHODS

A. Experimental details

A CIP-GMR spin-valve film consisting of $Co_{1-\beta}Fe_{\beta}$ (6 nm) /thickness-graded Cu (t_{Cu} = 1–5 nm)/$Co_{1-\beta}Fe_{\beta}$ (6 nm)/$Ir_{25}Mn_{75}$ (8 nm)/Ta (3 nm) was fabricated on a single-crystalline MgO (001) substrate using RF/DC magnetron sputtering with a combinatorial sputtering system (CMS-A6250X2, Comet Inc.). The direction of the composition gradient of the $Co_{1-\beta}Fe_{\beta}$ layer was designed to the *x*-direction of the substrate, while the thickness gradient of the Cu layer was set to the *y*-direction, allowing the complete dataset of Co–Fe composition and Cu film thickness dependence to be obtained on a single substrate [Fig. 1(g)]. The sputtering process was carried out at RT with a base pressure of less than 2.0×10^{-6} Pa. The deposition rate of Co, Fe, Cu, $Ir_{25}Mn_{75}$ ($IrMn_3$), and Ta was predetermined by x-ray reflectivity. Before layer deposition, the surface of a 20 × 20 mm^2 MgO (001) single-crystal substrate was subjected to a soft Ar-ion milling process within the sputtering chamber to clean the surface for epitaxial growth. The layer deposition process is

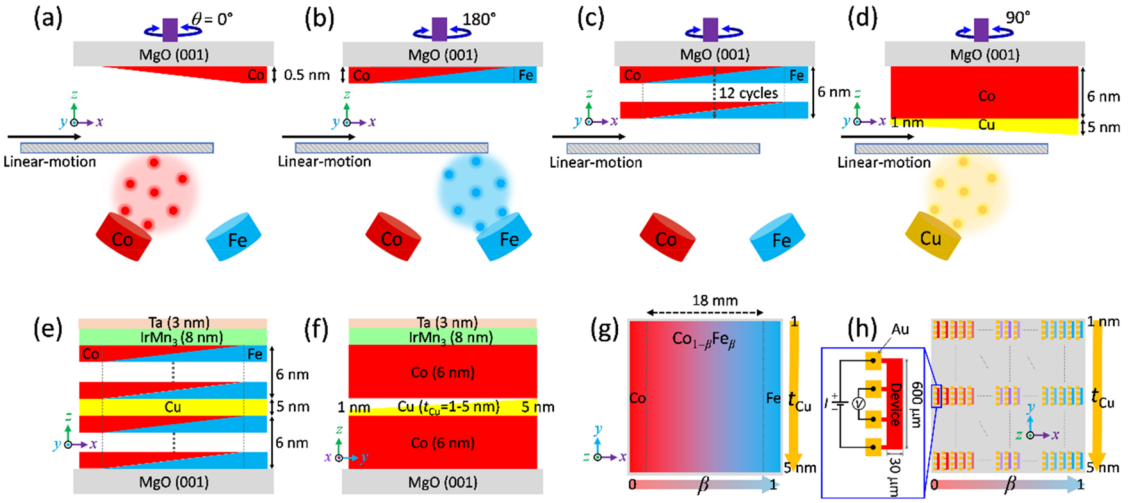

FIG. 1. A schematic illustration of the synthesis of a composition spread $Co_{1-\beta}Fe_{\beta}$/Cu/$Co_{1-\beta}Fe_{\beta}$-based CIP-GMR stack on a MgO (001) single-crystalline substrate. (a) A wedge-shaped Co layer deposition with a thickness of 0–0.5 nm. (b) 180° rotation of substrate and deposition of a wedge-shaped Fe layer with a thickness of 0–0.5 nm. After completing the processes (a) and (b), a uniform film layer with a thickness of 0.5 nm is obtained. A composition-spread film $Co_{1-\beta}Fe_{\beta}$ is obtained due to the intermixing of two compositions. (c) The processes (a) and (b) were repeated 12 times to complete a total thickness of 6 nm. (d) 90° rotation of substrate and deposition of a thickness-graded Cu spacer (t_{Cu} = 1–5 nm). (e) Schematic diagram of the CIP-GMR stack after depositing $IrMn_3$ (8 nm) and Ta (3 nm) layers (side view). (f) Thickness-graded Cu spacer at pure Co side. (g) Top view of the CIP-GMR stack with the variation of Co and Fe composition and Cu spacer thickness. (h) Multiple wire shape structures/devices with a four-terminal configuration and gold (Au)-coated electrodes. One of these structures can be seen in a zoomed-in view.

shown in Fig. 1. First, a composition-spread $Co_{1-\beta}Fe_\beta$ bottom layer with a thickness of 6 nm and composition variation over a length of 18 mm was deposited using pure Co and Fe targets. This layer was achieved using the following deposition sequence: (i) deposition of an ultra-thin wedge-shaped Co layer (0–0.5 nm) using a linear-motion mask [Fig. 1(a)], (ii) moving back of the mask and substrate rotation by 180°, and (iii) deposition of an ultra-thin wedge-shaped Fe layer (0–0.5 nm) using the linear-motion mask. The thickness of one-unit layer after the completion of processes (i)–(iii) was 0.5 nm [Fig. 1(b)]. As the thickness of each wedge layer is very small (0–0.5 nm), the intermixing of two compositions takes place, resulting in a composition gradient $Co_{1-\beta}Fe_\beta$ layer. The deposition sequence (i)–(iii) was repeated 12 times to reach a total thickness of 6 nm [Fig. 1(c)]. After that, the substrate was rotated by 90°, and a wedge-shaped Cu spacer layer with a thickness t_{Cu} of 1–5 nm was subsequently deposited over a length of 19 mm [Fig. 1(d)]. The substrate was then returned to its original angle (0°), and the processes (i)–(iii) were repeated to deposit the top $Co_{1-\beta}Fe_\beta$ (6 nm) layer [Fig. 1(c)]. Finally, an 8 nm-thick uniform $IrMn_3$ antiferromagnetic layer was deposited to pin the top $Co_{1-\beta}Fe_\beta$ layer, followed by a 3 nm-thick Ta capping layer to prevent oxidation [Fig. 1(e)]. The film stack was *ex situ* annealed at 250 °C, slightly higher than the blocking temperature of $IrMn_3$ (177 °C),[32] for 1 h in the presence of a constant in-plane external magnetic field of 0.3 T, oriented transverse to the $Co_{1-\beta}Fe_\beta$ composition spread (y-axis), to introduce the exchange bias to the top $Co_{1-\beta}Fe_\beta$ layer.

The local crystal structure of the film was analyzed by x-ray diffraction (XRD; SmartLab, Rigaku) with a Cu-K_α radiation source (wavelength λ = 1.5406 Å) at RT. The XRD data were collected at different local positions on the film along the composition gradient at an interval of 1.0 mm using a 0.5 mm incident slit. A two-dimensional (2D) detector was utilized to capture the 2D XRD images, and these images were subsequently converted into one-dimensional (1D) XRD patterns using dedicated instrument software (SmartLab Studio II, Rigaku). The XRD measurements provided structural information averaged over a 0.5 mm width, capturing a composition range of only ±1.3 at. %, which is sufficiently small for analyzing the composition dependence of MR. The film was then patterned into a four-terminal wire-shaped device with dimensions of 600 × 30 μm^2 and gold (Au)-coated electrodes with dimensions of 110 × 100 μm^2 using a standard photolithography and Ar-ion milling technique. A total of 1725 devices were fabricated, comprising 75 devices along the $Co_{1-\beta}Fe_\beta$ composition spread with a uniform spacing of 250 μm and 23 devices along the t_{Cu} wedge with an equal spacing of 800 μm [Fig. 1(h)]. Consequently, for each specific t_{Cu}, there are two wires in each pure region, i.e., pure Co (β = 0) and pure Fe (β = 1.0), while the remaining 71 wires are located in the composition spread region. The schematic diagram of the four-terminal wire shape devices is shown in a zoomed-in view [Fig. 1(h)]. It should be noted that the Co–Fe composition of each MR device was estimated based on its precise position along the composition gradient (Fig. S1 of the supplementary material). The MR of the patterned wires was efficiently measured at RT utilizing a semi-automatic prober system (Toei Scientific Industrial Co., Ltd., Japan) through a standard DC four-probe method. The applied magnetic field was swept along the long axis of four-terminal wires (y-axis) during the measurement.

B. First-principles calculations details

We have conducted first-principles calculations of the Fermi surface for bcc-$Co_{1-\beta}Fe_\beta$ and bcc-Cu at 0 K with a small step of β of 0.01 using the Vienna *Ab initio* Simulation Package (VASP) code.[33] The generalized gradient approximation (GGA) with the Perdew, Burke, and Ernzerhof (PBE) functional was employed for exchange–correlation energy calculations.[34] We used the virtual crystal approximation[35] for Co–Fe alloying in bcc-$Co_{1-\beta}Fe_\beta$, assuming a bcc structure for all compositions, including low β. A k-point grid of 20 × 20 × 20 was used with a broadening parameter of 0.1 eV. To analyze the effect of the change in the Fermi surface on the small change in the composition ratio of $Co_{1-\beta}Fe_\beta$, the calculations were performed with β in increments of 0.01. The lattice constant of bcc-$Co_{1-\beta}Fe_\beta$ changes from 2.832 to 2.866 Å as a function of β with Vegard's law, obtained from first-principles calculations.

III. RESULTS AND DISCUSSIONS

A. Structural analysis

Figure 2(a) shows 2θ–ω (out-of-plane, tilt angle χ = 0°) 1D XRD patterns of the $Co_{1-\beta}Fe_\beta$/Cu/$Co_{1-\beta}Fe_\beta$/$IrMn_3$/Ta CIP-GMR

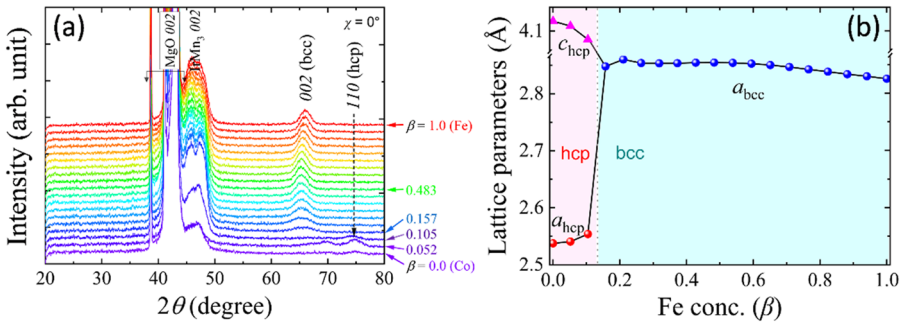

FIG. 2. (a) 1D XRD patterns (χ = 0°) converted from the 2D XRD images of the $Co_{1-\beta}Fe_\beta$/Cu/$Co_{1-\beta}Fe_\beta$-based CIP-GMR stacking film. (b) Fe concentration β dependence of the lattice constants (c_{hcp}, a_{hcp}, and a_{bcc}) calculated from the 101 (hcp), 110 (hcp), and 002 (bcc) XRD peak positions, respectively. [The 1D XRD patterns at $\chi \approx 40.2°$ for the 101 (hcp) peaks are presented for $\beta \leq 0.105$ (≈0.11) in Fig. S3(b) of the supplementary material.]

stack grown on a MgO (001) substrate with varying Fe concentration (β). The corresponding 2D XRD images can be found in Fig. S2 of the supplementary material. The $Co_{1-\beta}Fe_\beta$ layer exhibits diffraction peaks around $2\theta \approx 74.65°$ within the composition range up to approximately $\beta \leq 0.105 \approx 0.11$ ($Co_{0.89}Fe_{0.11}$), suggesting the possible presence of either hexagonal close-packed (hcp), face-centered cubic (fcc) or mixed (hcp + fcc) phases for $\beta \leq 0.11$. To investigate the origin of peaks around $2\theta \approx 74.65°$, we also conducted 2θ–ω (out-of-plane) XRD analysis at $\chi = 40.2°$ and the presence of 101 peaks at $2\theta \approx 46.80°$ revealed the hcp phase in the pure/rich Co composition ($\beta \leq 0.11$) [Fig. S3(b) of the supplementary material]. The observation of hcp phase in pure Co ($\beta = 0$) is consistent with the previous reports.[36–39] Upon surpassing $\beta \sim 0.11$, the 110 peak from the hcp phase disappears, and a 002 peak from the bcc structure emerges, indicating the structural transformation from a pure hcp to a pure bcc phase and the formation of a metastable bcc structure in Cu, as confirmed in previous studies[19,40] [Fig. 2(a)]. Unlike the previous report,[41] we did not detect any mixed phase in our sample. The spot-like shape of the 2D XRD images of all these diffraction peaks (Fig. S2 of the supplementary material) further supports the epitaxial nature in the whole β region of this sample. Furthermore, the 002 peak at $2\theta \approx 47°$ from $IrMn_3$ is observed continuously for all values of β in the XRD pattern due to the presence of $IrMn_3$ antiferromagnetic layer throughout the film area. The lattice constants, namely, c_{hcp}, a_{hcp}, and a_{bcc}, were calculated as a function of β from the peak positions of 101 (hcp), 110 (hcp), and 002 (bcc), respectively, shown in Fig. 2(b). These constants show a significant change in the vicinity of hcp-to-bcc phase transition (β ~0.11); however, they remain nearly persistent with β within their respective regions. c_{hcp} (a_{hcp}) and a_{bcc} were found to be ~4.12 Å (2.54 Å) and 2.83 Å for pure Co ($\beta = 0$) and pure Fe ($\beta = 1.0$), respectively, which are comparable to the previous reports.[39,42]

To examine whether the presence of hcp Co lattice distorts the bcc-$Co_{1-\beta}Fe_\beta$ structure for $\beta > 0.11$, we calculated the lattice parameter (c_1) using the 110 (bcc) diffraction peaks for $\beta = 0.157$, 0.211, and 0.264 [Fig. S3(c) of the supplementary material]. It was found that both c_1 and a ($\equiv a_{bcc}$) remain nearly equal and constant for these β values. As a result, the c_1/a ratio remains close to unity, indicating that the presence of hcp Co lattice does not distort the bcc-$Co_{1-\beta}Fe_\beta$ structure. This further suggests that a single lattice parameter a_{bcc} is sufficient to describe the $Co_{1-\beta}Fe_\beta$ structure for $\beta > 0.11$.

B. Magnetoresistance (MR) effect

Figure 3(a) displays typical MR curves plotted against the magnetic field (H) measured at RT for $Co_{1-\beta}Fe_\beta$/Cu/$Co_{1-\beta}Fe_\beta$-based CIP-GMR devices for a fixed t_{Cu} = 1.36 nm. These curves clearly reveal the parallel (P) and antiparallel (AP) states existing between the top and bottom $Co_{1-\beta}Fe_\beta$ layers, which are separated by the Cu spacer. It is worth noting that the exchange bias effect using $IrMn_3$ realized clear AP states in all devices having enough thick Cu spacer to remove a direct magnetic coupling between $Co_{1-\beta}Fe_\beta$ layers ($t_{Cu} \gtrsim 1.3$ nm). Due to the dominant contribution of the exchange bias effect in the AP state, the AP state is not disrupted by ferromagnetic and antiferromagnetic interlayer exchange couplings, which are expected to appear with Cu thickness oscillatory. To provide a clear view of the AP states within these devices, an MR curve is included in the inset of Fig. 3(a) for the specific conditions of t_{Cu} = 1.36 nm and $\beta = 0.37$. Here, the MR ratio (%) is defined as $(R_{AP} - R_P)/R_P \times 100\%$, where R_{AP} and R_P are the resistances for the AP and P configurations of the top and bottom $Co_{1-\beta}Fe_\beta$ layers, respectively. Such MR analyses for $Co_{1-\beta}Fe_\beta$/Cu(t_{Cu})/$Co_{1-\beta}Fe_\beta$ were performed for various Cu thicknesses ranging from 1 to 5 nm. Figure 3(b) illustrates the contour color plot of the MR ratio as a function of both β and t_{Cu}. A distinct variation in the MR ratio is observed with changing β and t_{Cu}. It is observed that the MR ratio increases sharply when the Cu spacer reaches a threshold thickness of ~1.18 nm and reaches its highest value at t_{Cu} = 1.36 nm. This is because of the direct magnetic contact of two $Co_{1-\beta}Fe_\beta$ layers disturbing the AP configuration with the too thin Cu layer. Beyond the peak thickness, the MR ratio decreases sharply as the increase in the shunting current in Cu spacer loses the spin-dependent scattering, resulting in a reduction in the MR ratio. Notably, the highest MR ratio is observed in the vicinity of $\beta = 0.50$ ($Co_{0.50}Fe_{0.50}$), which is consistent with the previous report.[19] In particular, β = 0.46

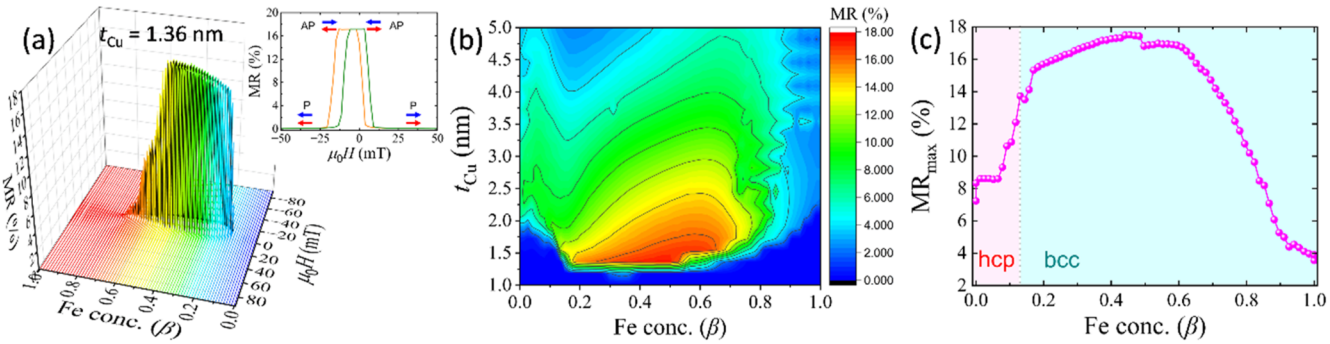

FIG. 3. (a) MR curves against the magnetic field (H) measured at RT for $Co_{1-\beta}Fe_\beta$/Cu/$Co_{1-\beta}Fe_\beta$-based CIP-GMR devices at fixed Cu thickness t_{Cu} = 1.36 nm. The inset shows a typical MR curve (t_{Cu} = 1.36 nm, $\beta = 0.37$), exhibiting AP and P states. (b) The contour color plot of MR ratio (%) measured at RT as a function of Cu thickness (t_{Cu}) and Fe concentration (β). (c) Fe concentration β dependence of the *maximum* MR (MR_{max}) ratio, without considering the specific Cu thickness at which the maximum MR was achieved.

($Co_{0.54}Fe_{0.46}$) exhibits the highest MR ratio of 17.5% at t_{Cu} = 1.36 nm; however, this value is lower than the previously reported[19] MR ratio of 26.5%. The relatively diminished MR ratio could be attributed to inferior microstructural factors, such as interfacial roughness and grain sizes.[43–48]

To better depict the dependence of the MR ratio on Fe concentration β, we have plotted the *maximum* MR (MR_{max}) ratio as a function of β, without considering the specific Cu thickness at which the maximum MR was achieved, as shown in Fig. 3(c). MR_{max} was found to increase largely at $\beta > 0.11$, just above the hcp-to-bcc phase transition region, and attained its highest value at $\beta = 0.46$. It is worth highlighting that within the range of $0.11 < \beta \leq 1.0$, despite exhibiting an identical (bcc) crystal structure and a clear AP magnetization state, a significant decline in the MR ratio from 17% to 4% occurred from around $\beta = 0.60$ to 1.0 (pure Fe).

To investigate whether the device resistance influences the MR results, we extracted the resistance R_P of the CIP-GMR devices from their MR curves across all Cu thicknesses (t_{Cu} = 1–5 nm), displayed in Fig. S4 of the supplementary material. The nonlinear variation of R_P as a function of β is consistent with the previous study.[49] While higher (lower) device resistance can reduce (enhance) the MR ratio, our observations indicate that neither the MR ratio nor MR_{max} accurately follows the variation of R_P with changes in β. These observations suggest that device resistance has a minor influence on MR results, while the variation in EBM with β mentioned below plays a dominant role.

The observed variation in the MR ratio with composition is expected to originate from the interfacial EBM between bcc Co–Fe and bcc-Cu[19,21] because it is known that the interfacial spin-dependent electron scattering is much more dominant for the MR effect than the bulk scattering.[50] In a previous study,[19] it was elucidated by first-principles calculations that the ballistic transmittance in a two-dimensional $k_{//}$-plane for $Co_{50}Fe_{50}$/bcc-Cu/$Co_{50}Fe_{50}$ (Fe/bcc-Cu/Fe) exhibits a key feature: a large (small) transmittance of majority-spin electrons at around the BZ edge correlates with a high (low) MR ratio. To gain insights into the underlying mechanism influencing the MR ratio as a function of β without performing a time-consuming calculation of the transmittance, we have here

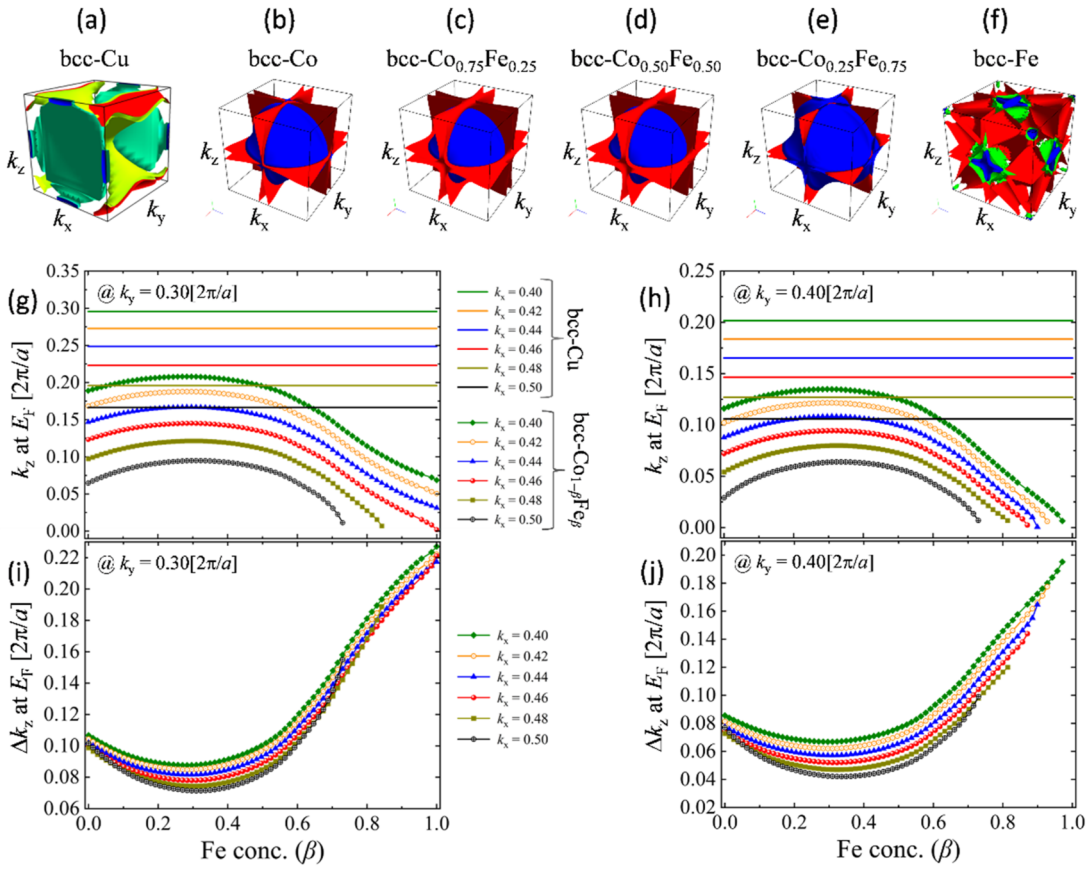

FIG. 4. Fermi surfaces in the Brillouin zones (BZs) corresponding to (a) bcc-Cu, (b) bcc-Co, (c) bcc-$Co_{0.75}Fe_{0.25}$, (d) bcc-$Co_{0.50}Fe_{0.50}$, (e) bcc-$Co_{0.25}Fe_{0.75}$, and (f) bcc-Fe. Band dispersion in the k_z direction along [001] as a function of Fe concentration β in bcc-$Co_{1-\beta}Fe_\beta$ and bcc-Cu for k_x = 0.40, 0.42, 0.44, 0.46, 0.48, and 0.50[2π/*a*] at (g) k_y = 0.30[2π/*a*], and (h) k_y = 0.40[2π/*a*]. *a* denotes the lattice constant of the unit cell. The solid horizontal line indicates the k_z value for bcc-Cu at the corresponding k_x and k_y. The difference of k_z between bcc-$Co_{1-\beta}Fe_\beta$ and bcc-Cu, $\Delta k_z = k_z^{Cu} - k_z^{CoFe}$, as a function of Fe concentration at (i) k_y = 0.30[2π/*a*] and (j) k_y = 0.40[2π/*a*].

performed first-principles calculations of the Fermi surface of bcc-Cu and the majority-spin of $Co_{1-\beta}Fe_\beta$ with β varying at intervals of ~0.01. It is worth noting that for the sake of simplicity in our analysis of the EBM, we considered only the majority-spin electrons of $Co_{1-\beta}Fe_\beta$, which have been shown to have significantly higher transmittance than minority-spin electrons in the study of $Co_{50}Fe_{50}$.[19] $Co_{1-\beta}Fe_\beta$ was assumed to be crystallized in the bcc phase even for $\beta < 0.16$. Figures 4(a)–4(f) show the calculated Fermi surfaces for bcc-Cu and bcc $Co_{1-\beta}Fe_\beta$ (β = 0, 0.25, 0.50, 0.75, 1.00). It is clear that only Fe (β = 1.0) has a largely different shape of the Fermi surface from the other compositions. To investigate the in-plane transport properties governed by the electron having a large $k_{//}$ near the BZ edge, we analyzed the similarity of the Fermi surfaces between bcc-$Co_{1-\beta}Fe_\beta$ and bcc-Cu from the distance of k_z (z-component of the wave vector k crossing the Fermi level) value at the specific (k_x, k_y) points. Namely, we analyzed k_z for in-plane wave vector k_x = 0.40, 0.42, 0.44, 0.46, 0.48, and 0.50[2π/a] at k_y = 0.30[2π/a] and k_y = 0.40[2π/a], where significant changes in transmittance between $Co_{50}Fe_{50}$ and Fe were observed in the previous study.[19] Here, a represents the lattice constant of the unit cell. In Figs. 4(g) and 4(h), the variation of k_z of bcc-$Co_{1-\beta}Fe_\beta$ as a function of β and the k_z of bcc-Cu at different k_x are depicted for k_y = 0.30[2π/a] and k_y = 0.40[2π/a], respectively. It is evident that a clear change occurs in k_z with varying β, indicating a large difference in k_z between bcc-$Co_{1-\beta}Fe_\beta$ and bcc-Cu as a function of β.

To evaluate the EBM between bcc-$Co_{1-\beta}Fe_\beta$ and bcc-Cu at the specific (k_x, k_y) points, we calculated the difference in k_z values as Δk_z (k_x, k_y) = $k_z^{Cu}(k_x, k_y) - k_z^{CoFe}(k_x, k_y)$. The calculated Δk_z for both k_y values is shown in Figs. 4(i) and 4(j). Here, Δk_z = 0 indicates perfect matching of the Fermi surfaces at this specific k-point. Note that there are several ways to estimate the distance between two Fermi surfaces in the k-space, such as taking the radial or Euclidean distance. However, in this study, we follow the previous study[19] in which the authors plotted the band dispersion to the k_z direction at the specific (k_x, k_y) points of bcc Cu, $Co_{50}Fe_{50}$, and Fe and analyzed the similarity. We observed that Δk_z slowly decreases as β increases from 0 and reaches its nearly flat bottom region with a small slope around β = 0.20–0.50, suggesting a favorable EBM condition in this composition range. However, with further increments in β over 0.60, Δk_z begins to increase rapidly, indicating a diminished EBM between bcc-$Co_{1-\beta}Fe_\beta$ and bcc-Cu at these (k_x, k_y). Notably, these calculated results are consistent with our experimental results, where the highest MR_{max} ratio was observed around β = 0.46, and a rapid reduction in the MR ratio was observed with increasing β beyond 0.60 [Fig. 3(c)]. To enhance the visibility of the difference between our computed Δk_z and the experimentally measured MR_{max} with respect to β, we calculated their derivatives, namely, $d(\Delta k_z)/d\beta$ and $d(MR_{max})/d\beta$, which are presented in Figs. 5(a) and 5(b), respectively. These derivatives shed light on the variation of Δk_z and MR_{max} as a function of β. It is important to note that $d(MR_{max})/d\beta$ was calculated only for the bcc phase region ($\beta \geq 0.16$). Interestingly, we observed a clear qualitative similarity: both $d(\Delta k_z)/d\beta$ and $d(MR_{max})/d\beta$ are small in the range of β from 0.20 to 0.50, specifically between −0.2 and 0.1, and share a common inflection point around β = 0.70–0.80. This raises the question: does the change in MR_{max} ratio truly originate from the EBM or influenced by changes in the quality of the crystal structure? The characterization of broadening (ω) of the 002 (bcc) peaks (Fig. S5 of the supplementary material) ruled out the possibility that the change in MR_{max} ratio was due to the variation in the quality of the crystal structure. This observation strongly suggests that the change in MR_{max} ratio primarily originates from the factors associated with EBM rather than the change in the quality of the crystal structure.

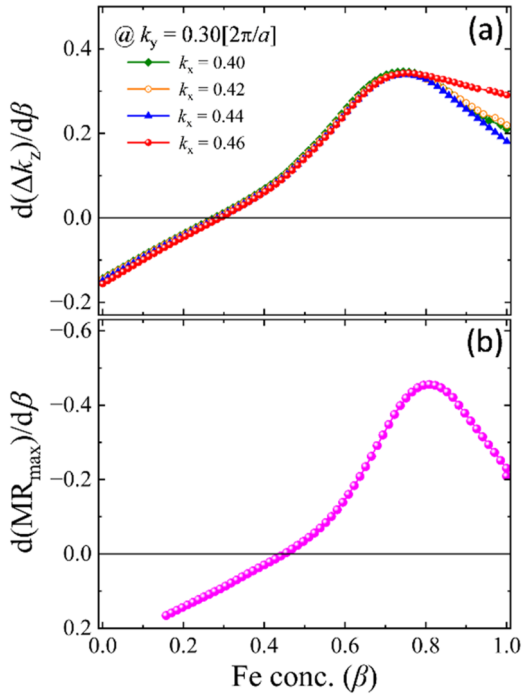

FIG. 5. Derivatives of Δk_z and MR_{max} with respect to β: (a) $d(\Delta k_z)/d\beta$ at k_y = 0.30[2π/a] and (b) $d(MR_{max})/d\beta$. Here, $d(\Delta k_z)/d\beta$ for k_x = 0.48 and 0.50 were omitted due to the absence of data points beyond $\beta \approx 0.80$. The derivative of MR_{max} [not in MR_{max} (%)] was specifically calculated for the bcc region ($\beta \geq 0.16$) only. Please observe the contrasting directions of the scales in (a) and (b).

These findings on the Co–Fe/Cu CIP-GMR model system suggest that the analysis of Fermi surface matching can be utilized to predict the spin-dependent transport properties of heterojunctions of magnetic and non-magnetic materials. Since the calculation of Fermi surface requires much less computational time than the ballistic transmittance, this approach can efficiently generate a large amount of data suitable for machine learning. This dataset can be used to predict/optimize the stacking structures to achieve enhanced MR effects in both CIP-GMR and CPP-GMR devices. As an initial step in developing a new method that combines machine learning and first-principles calculations to explore material combinations, this study involved a manual analysis of the Fermi surface similarity at specific k-points between Co–Fe and Cu. Therefore, based on the results of the present study, the next important step is to develop a new method that can automatically examine the similarity of Fermi surfaces in a wide/full region of k-space for other material systems having different structures, such as fcc and hcp. A possible strategy could involve unsupervised machine learning techniques, such as cluster analysis and dimensionality reduction, to analyze Fermi

surface similarities. This is an ongoing study and will be reported in the future.

IV. CONCLUSIONS

In conclusion, we have effectively investigated the effect of EBM at the interface of $Co_{1-\beta}Fe_\beta$/Cu/$Co_{1-\beta}Fe_\beta$ based CIP-GMR devices on the MR ratio using a combinatorial deposition technique for the epitaxial CIP-GMR structure. This approach generated a comprehensive dataset of MR ratios covering the entire spectrum of $Co_{1-\beta}Fe_\beta$ compositions and Cu thicknesses. Our findings showed a significant variation in the MR ratio in the range of β = 0.11–1.0, despite identical crystallinity and a clear antiparallel magnetization state. In particular, the highest MR was observed in the vicinity of $\beta \approx 0.46$ and a rapid decrease occurred with increasing β beyond 0.60. To understand this β dependence of the MR ratio, we performed first-principles calculations at low computational cost, calculating the Fermi surface of bcc-Cu and the majority-spin of bcc-$Co_{1-\beta}Fe_\beta$ and comparing their similarities. We found that the difference in the k_z values of the Fermi surfaces is minimal in the region of $\beta \approx 0.20$–0.50 and increases monotonically with β above 0.60. This trend is in good agreement with the experimental β dependence of the MR ratio. These results demonstrate the effectiveness of analyzing Fermi surface similarities between ferromagnetic and non-magnetic materials to predict the spin-dependent transport properties of various magnetic/non-magnetic heterojunctions at low computational cost, which can be beneficially combined with machine learning techniques in the future.

SUPPLEMENTARY MATERIAL

The supplementary material encompasses the Co–Fe composition calculation method, 1D and 2D XRD results, and the resistance of CIP-GMR devices.

ACKNOWLEDGMENTS

The authors thank T. Hiroto for providing technical support during the XRD measurements. This research was financially supported by JSPS KAKENHI under Grant No. 19K05249, JST CREST under Grant No. JPMJCR21O1, and the MEXT Program: Data Creation and Utilization-Type Material Research and Development Project (Digital Transformation Initiative Center for Magnetic Materials) under Grant No. JPMXP1122715503 in Japan. The calculations and x-ray diffraction measurement in this study were preformed on the Numerical Materials Simulator and Surface and Bulk Analysis Unit in NIMS, respectively.

AUTHOR DECLARATIONS

Conflict of Interest

The authors have no conflicts to disclose.

Author Contributions

Varun Kumar Kushwaha: Data curation (lead); Formal analysis (lead); Investigation (lead); Validation (lead); Writing – original draft (lead); Writing – review & editing (lead). **Ryo Toyama**: Formal analysis (equal); Investigation (supporting); Writing – review & editing (supporting). **Yoshio Miura**: Conceptualization (equal); Data curation (equal); Formal analysis (equal); Investigation (supporting); Writing – original draft (supporting). **Yuma Iwasaki**: Funding acquisition (lead); Methodology (equal); Writing – review & editing (supporting). **Yuya Sakuraba**: Conceptualization (lead); Funding acquisition (lead); Methodology (equal); Resources (equal); Supervision (lead); Writing – review & editing (lead).

DATA AVAILABILITY

The data that support the findings of this study are available from the corresponding authors upon reasonable request.

REFERENCES

[1] Y. Iwasaki, R. Sawada, E. Saitoh, and M. Ishida, "Machine learning autonomous identification of magnetic alloys beyond the Slater-Pauling limit," Commun. Mater. **2**, 31 (2021).
[2] Y. Iwasaki, H. Jaekyun, Y. Sakuraba, M. Kotsugi, and Y. Igarashi, "Efficient autonomous material search method combining *ab initio* calculations, autoencoder, and multi-objective Bayesian optimization," Sci. Technol. Adv. Mater.: Methods **2**, 365–371 (2022).
[3] K. Takahashi, L. Takahashi, I. Miyazato, and Y. Tanaka, "Searching for hidden perovskite materials for photovoltaic systems by combining data science and first principle calculations," ACS Photonics **5**, 771–775 (2018).
[4] R. Shimizu, S. Kobayashi, Y. Watanabe, Y. Ando, and T. Hitosugi, "Autonomous materials synthesis by machine learning and robotics," APL Mater. **8**, 111110 (2020).
[5] D. Furuya, T. Miyashita, Y. Miura, Y. Iwasaki, and M. Kotsugi, "Autonomous synthesis system integrating theoretical, informatics, and experimental approaches for large-magnetic-anisotropy materials," Sci. Technol. Adv. Mater.: Methods **2**, 280–293 (2022).
[6] N. J. Szymanski, Y. Zeng, H. Huo, C. J. Bartel, H. Kim, and G. Ceder, "Toward autonomous design and synthesis of novel inorganic materials," Mater. Horiz. **8**, 2169–2198 (2021).
[7] P. Nikolaev, D. Hooper, F. Webber, R. Rao, K. Decker, M. Krein, J. Poleski, R. Barto, and B. Maruyama, "Autonomy in materials research: A case study in carbon nanotube growth," Npj Comput. Mater. **2**, 16031 (2016).
[8] A. Seko, A. Togo, H. Hayashi, K. Tsuda, L. Chaput, and I. Tanaka, "Prediction of low-thermal-conductivity compounds with first-principles anharmonic lattice-dynamics calculations and Bayesian optimization," Phys. Rev. Lett. **115**, 205901 (2015).
[9] R. Sawada, Y. Iwasaki, and M. Ishida, "Boosting material modeling using game tree search," Phys. Rev. Mater. **2**, 103802 (2018).
[10] J. M. Granda, L. Donina, V. Dragone, D.-L. Long, and L. Cronin, "Controlling an organic synthesis robot with machine learning to search for new reactivity," Nature **559**, 377–381 (2018).
[11] I. Kurniawan, Y. Miura, and K. Hono, "Machine learning study of highly spin-polarized Heusler alloys at finite temperature," Phys. Rev. Mater. **6**, L091402 (2022).
[12] K. M. Schep, P. J. Kelly, and G. E. W. Bauer, "Giant magnetoresistance without defect scattering," Phys. Rev. Lett. **74**, 586–589 (1995).
[13] M. D. Stiles and D. R. Penn, "Calculation of spin-dependent interface resistance," Phys. Rev. B **61**, 3200–3202 (2000).
[14] K. Carva and I. Turek, "Spin-mixing conductances of thin magnetic films from first principles," Phys. Rev. B **76**, 104409 (2007).
[15] V. Ko, G. Han, J. Qiu, and Y. P. Feng, "The band structure-matched and highly spin-polarized Co_2CrZ/Cu_2CrAl Heusler alloys interface," Appl. Phys. Lett. **95**, 202502 (2009).
[16] Y. Sakuraba, K. Izumi, T. Iwase, S. Bosu, K. Saito, K. Takanashi, Y. Miura, K. Futatsukawa, K. Abe, and M. Shirai, "Mechanism of large magnetoresistance in $Co_2MnSi/Ag/Co_2MnSi$ devices with current perpendicular to the plane," Phys. Rev. B **82**, 094444 (2010).

[17]Y. Liu, Z. Yuan, R. J. H. Wesselink, A. A. Starikov, and P. J. Kelly, "Interface enhancement of Gilbert damping from first principles," Phys. Rev. Lett. **113**, 207202 (2014).
[18]T. Kubota, Y. Ina, M. Tsujikawa, S. Morikawa, H. Narisawa, Z. Wen, M. Shirai, and K. Takanashi, "Current perpendicular-to-plane giant magnetoresistance devices using half-metallic $Co_2Fe_{0.4}Mn_{0.6}Si$ electrodes and a Ag–Mg spacer," J. Phys. D Appl. Phys. **50**, 014004 (2017).
[19]K. B. Fathoni, Y. Sakuraba, T. Sasaki, Y. Miura, J. W. Jung, T. Nakatani, and K. Hono, "Band match enhanced current-in-plane giant magnetoresistance in epitaxial $Co_{50}Fe_{50}$/Cu multilayers with metastable bcc-Cu spacer," APL Mater. **7**, 111106 (2019).
[20]Y. Fujita, Y. Miura, T. Sasaki, T. Nakatani, K. Hono, and Y. Sakuraba, "Spin-scattering asymmetry at half-metallic-ferromagnet|ferromagnet interface," Phys. Rev. B **104**, L140403 (2021).
[21]K. B. Fathoni, Y. Sakuraba, Y. Miura, T. Sasaki, T. Nakatani, and K. Hono, "Analysis of current-in-plane giant magnetoresistance using $Co_2FeAl_{0.5}Si_{0.5}$ half-metallic Heusler alloy," J. Phys. D Appl. Phys. **55**, 125001 (2022).
[22]T. Valet and A. Fert, "Theory of the perpendicular magnetoresistance in magnetic multilayers," Phys. Rev. B **48**, 7099–7113 (1993).
[23]Combinatorial Technology, Comet Inc. https://www.comet-nht.com/concepte.html.
[24]R. Modak, K. Goto, S. Ueda, Y. Miura, K. Uchida, and Y. Sakuraba, "Combinatorial tuning of electronic structure and thermoelectric properties in $Co_2MnAl_{1-x}Si_x$ Weyl semimetals," APL Mater. **9**, 031105 (2021).
[25]R. Toyama, S. Kokado, K. Masuda, Z. Li, V. K. Kushwaha, T. T. Sasaki, L. S. R. Kumara, T. Koganezawa, H. Tajiri, T. Yamazaki, M. Kotsugi, Y. Iwasaki, and Y. Sakuraba, "Origin of negative anisotropic magnetoresistance effect in $Fe_{0.75}Co_{0.25}$ single-crystal thin films upon Ir addition," Phys. Rev. Mater. **7**, 084401 (2023).
[26]H. Masuda, R. Modak, T. Seki, K. Uchida, Y.-C. Lau, Y. Sakuraba, R. Iguchi, and K. Takanashi, "Large spin-Hall effect in non-equilibrium binary copper alloys beyond the solubility limit," Commun. Mater. **1**, 75 (2020).
[27]I. Takeuchi, O. O. Famodu, J. C. Read, M. A. Aronova, K.-S. Chang, C. Craciunescu, S. E. Lofland, M. Wuttig, F. C. Wellstood, L. Knauss, and A. Orozco, "Identification of novel compositions of ferromagnetic shape-memory alloys using composition spreads," Nat. Mater. **2**, 180–184 (2003).
[28]H. Koinuma and I. Takeuchi, "Combinatorial solid-state chemistry of inorganic materials," Nat. Mater. **3**, 429–438 (2004).
[29]R. Toyama, V. K. Kushwaha, T. T. Sasaki, Y. Iwasaki, T. Nakatani, and Y. Sakuraba, "Combinatorial optimization for high spin polarization in Heusler alloy composition-spread thin films by anisotropic magnetoresistance effect," APL Mater. **11**, 101127 (2023).
[30]R. Toyama, W. Zhou, and Y. Sakuraba, "Extrinsic contribution to the anomalous Hall effect and Nernst effect in Fe_3Co single-crystal thin films by Ir doping," Phys. Rev. B **109**, 054415 (2024).
[31]V. Barwal, H. Suto, T. Taniguchi, and Y. Sakuraba, "Detailed and high-throughput measurement of composition dependence of magnetoresistance and spin–transfer torque using a composition-gradient film: Application to Co_xFe_{1-x} ($0 \le x \le 1$) system," Sci. Technol. Adv. Mater.:Methods **3**, 2286944 (2023).
[32]E. Z. Zhang, Y. C. Deng, X. H. Liu, X. Z. Zhan, T. Zhu, and K. Y. Wang, "Manipulating antiferromagnetic interfacial states by spin-orbit torques," Phys. Rev. B **104**, 134408 (2021).
[33]G. Kresse and J. Furthmüller, "Efficient iterative schemes for *ab initio* total-energy calculations using a plane-wave basis set," Phys. Rev. B **54**, 11169–11186 (1996).
[34]J. P. Perdew, K. Burke, and M. Ernzerhof, "Generalized gradient approximation made simple," Phys. Rev. Lett. **77**, 3865–3868 (1996).
[35]L. Bellaiche and D. Vanderbilt, "Virtual crystal approximation revisited: Application to dielectric and piezoelectric properties of perovskites," Phys. Rev. B **61**, 7877–7882 (2000).
[36]Y. Nukaga, M. Ohtake, M. Futamoto, F. Kirino, N. Fujita, and N. Inaba, "Structure and magnetic properties of Co epitaxial thin films grown on MgO single-crystal substrates," IEEE Trans. Magn. **45**, 2519–2522 (2009).
[37]Y. V. Goryunov, M. G. Khusainov, I. A. Garifullin, F. Schreiber, J. Pelzl, T. Zeidler, K. Bröhl, N. Metoki, and H. Zabel, "FMR study of MBE-grown Co films on Al_2O_3 and MgO substrates," J. Magn. Magn. Mater. **138**, 216–221 (1994).
[38]O. Kohmoto, H. Kitamura, T. Tsuda, and F. Ono, "Magnetic properties of sputtered Co films," Phys. Status Solidi A **176**, 1039–1045 (1999).
[39]M. Ohtake, O. Yabuhara, J. Higuchi, and M. Futamoto, "Preparation and characterization of Co single-crystal thin films with hcp, fcc and bcc structures," J. Appl. Phys. **109**, 07C105 (2011).
[40]B. Heinrich, Z. Celinski, J. F. Cochran, W. B. Muir, J. Rudd, Q. M. Zhong, A. S. Arrott, K. Myrtle, and J. Kirschner, "Ferromagnetic and antiferromagnetic exchange coupling in bcc epitaxial ultrathin Fe(001)/Cu(001)Fe(001) trilayers," Phys. Rev. Lett. **64**, 673–676 (1990).
[41]M. A. W. Schoen, J. Lucassen, H. T. Nembach, T. J. Silva, B. Koopmans, C. H. Back, and J. M. Shaw, "Magnetic properties of ultrathin 3*d* transition-metal binary alloys. I. Spin and orbital moments, anisotropy, and confirmation of Slater-Pauling behavior," Phys. Rev. B **95**, 134410 (2017).
[42]H. Kronmuller and S. Parkin, *Handbook of Magnetism and Advanced Magnetic Materials* (John Wiley & Sons Ltd., 2007), Vol. 1.
[43]A. Gupta, A. Paul, S. M. Chaudhari, and D. M. Phase, "Effect of interface roughness on GMR in Fe/Cr multilayers," J. Phys. Soc. Jpn. **69**, 2182–2187 (2000).
[44]V. A. Vas'ko and M. T. Kief, "Effect of grain size on the properties of the CoFe–NiFe/NiMn top spin valve," J. Appl. Phys. **93**, 8409–8411 (2003).
[45]X. Peng, A. Morrone, K. Nikolaev, M. Kief, and M. Ostrowski, "Effect of material selection and background impurity on interface property and resulted CIP-GMR performance," J. Magn. Magn. Mater. **321**, 2902–2910 (2009).
[46]M. Milyaev, L. Naumova, V. Proglyado, T. Krinitsina, N. Bannikova, and V. Ustinov, "High GMR effect and perfect microstructure in CoFe/Cu multilayers," IEEE Trans. Magn. **55**, 1–4 (2019).
[47]P. D. Kulkarni, T. Nakatani, T. Sasaki, and Y. Sakuraba, "Effects of $(Ni_{0.8}Fe_{0.2})_{100-x}Cr_x$ seed layer on microstructure, magnetic properties, and giant magnetoresistance of [FeCoNi/Cu] multilayer films," J. Appl. Phys. **129**, 213901 (2021).
[48]M. El Harfaoui, H. Le Gall, J. Ben Youssef, S. Pogossian, A. Thiaville, P. Gogol, A. Qachaou, and J. Desvignes, "GMR versus interfacial roughness induced from different buffers in (Co/Cu) ML," J. Magn. Magn. Mater. **198–199**, 107–109 (1999).
[49]P. P. Freitas and L. Berger, "Effect of atomic order on the electrical resistivity of Co_xFe_{100-x} alloys," Phys. Rev. B **37**, 6079–6084 (1988).
[50]B. Dieny, "Giant magnetoresistance in spin-valve multilayers," J. Magn. Magn. Mater. **136**, 335–359 (1994).